


Article

UV-Activated NO₂ Gas Sensing by Nanocrystalline ZnO: Mechanistic Insights from Mass Spectrometry Investigations

Artem Chizhov¹, Pavel Kutukov¹ , Alexander Gulin², Artyom Astafiev² and Marina Rumyantseva^{1,*} 

¹ Chemistry Department, Moscow State University, 119991 Moscow, Russia; chizhov@inorg.chem.msu.ru (A.C.); pavel.kutukov@chemistry.msu.ru (P.K.)

² N.N. Semenov Federal Research Center, Chemical Physics of Russian Academy of Sciences, 119991 Moscow, Russia; aleksandr.gulin@phystech.edu (A.G.); astafiev.artyom@gmail.com (A.A.)

* Correspondence: room@inorg.chem.msu.ru; Tel.: +7-(495)-939-4664

Abstract: In this work, the photostimulated processes of O₂ and NO₂ molecules with the surface of ZnO under UV radiation were studied by in situ mass spectrometry in the temperature range of 30–100 °C. Nanocrystalline needle-like ZnO was synthesized by decomposition of basic zinc carbonate at 300 °C, and the surface concentration of oxygen vacancies in it were controlled by reductive post-annealing in an inert gas at 170 °C. The synthesized materials were characterized by XRD, SEM, low-temperature nitrogen adsorption (BET), XPS, Raman spectroscopy, and PL spectroscopy. Irradiation of samples with UV light causes the photoabsorption of both O₂ and NO₂. The photoadsorption properties of ZnO are compared with its defective structure and gas-sensitive properties to NO₂. A model of the sensor response of ZnO to NO₂ under UV photoactivation is proposed.

Keywords: gas sensor; photoactivation; ZnO; mass spectrometry; nanomaterials



Citation: Chizhov, A.; Kutukov, P.; Gulin, A.; Astafiev, A.; Rumyantseva, M. UV-Activated NO₂ Gas Sensing by Nanocrystalline ZnO: Mechanistic Insights from Mass Spectrometry Investigations. *Chemosensors* **2022**, *10*, 147. <https://doi.org/10.3390/chemosensors10040147>

Academic Editors: Valerio Vignoli and Enza Panzardi

Received: 24 March 2022

Accepted: 13 April 2022

Published: 15 April 2022

Publisher's Note: MDPI stays neutral with regard to jurisdictional claims in published maps and institutional affiliations.



Copyright: © 2022 by the authors. Licensee MDPI, Basel, Switzerland. This article is an open access article distributed under the terms and conditions of the Creative Commons Attribution (CC BY) license (<https://creativecommons.org/licenses/by/4.0/>).

1. Introduction

The effect of atmospheric composition on the electrical conductivity of metal oxides has been known since the 1950s [1]. This discovery marked the beginning of the development of resistive-type gas sensors, which are known by their simplicity of design, low cost, and high sensitivity. To date, many efforts have been made to improve the selectivity, sensitivity, response, and recovery rates of resistive-type metal oxide sensors [2–7]. One of the weaknesses of metal oxide gas sensors is their low energy efficiency, since in most cases, to activate the sensor response, the sensitive layer should be heated to a temperature of 200–500 °C. However, high operating temperature leads to high energy consumption, early degradation of the sensitive layer due to accelerated diffusion and recrystallization processes, and fire and explosion hazards.

One of the well-known trends in reducing the operating temperature and power consumption of metal oxide sensors that have been actively developed in the last decade is the use of ultraviolet (UV) or visible light activation instead of thermal activation [8–11]. This approach has already proven its effectiveness in the room-temperature (RT) detection of some organic vapors [12] and especially oxidizing gases such as O₃ and NO₂ [9,13–16]. However, the mechanism of gas sensitivity of metal oxide gas sensors under light activation in most cases remains controversial. Attempts to build a gas-sensitivity model only based on the analysis of the in situ conductivity of the sensor often lead to ambiguous results, since the electrical conductivity of nanosized metal oxides is totally valued depending on many parameters, and all of them can hardly be taken into account. The development of a comprehensive model of chemical gas sensitivity is impossible without using additional in situ and operando research methods that allow independent identification of interacting particles on the surface of metal oxides. Examples of such studies involve in situ XPS spectroscopy [17,18], in situ IR-spectroscopy [19,20], in situ Raman spectroscopy [21], in situ EPR [22], and other methods [23] for obtaining more detailed information on the

mechanism of gas sensitivity of metal oxides. Despite the intensive work carried out in this direction, the gap is still large.

The RT sensitivity of ZnO-based sensors in NO₂ detection under UV illumination is an illustrative example of how the replacement of thermal activation with light activation can achieve an impressive sensitivity at the ppb level [24,25]. Intensive research into the mechanisms of light-activated gas sensitivity also focused on ZnO-based materials [26,27]. Promising approaches have been developed to improve the gas-sensitive properties of ZnO by engineering of oxygen vacancies [22,28–35].

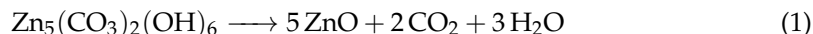
To complement and expand these studies, we proposed to use mass spectrometry (MS) for more detailed investigation of the mechanisms of photoactivation processes on the surface of metal oxides, which contribute to sensor sensitivity. MS is a powerful and sensitive experimental tool that allows to identify species involved in chemical reactions and track changes in their concentration, which was shown, for example, in the studies of some photocatalytic processes [36,37].

In this work we carried out an MS study of photoactivated processes on the ZnO surface when interacting with O₂ and NO₂ molecules. Then, we compared the data obtained with the gas-sensitive characteristics of synthesized ZnO samples. Annealing in an inert gas was used to adjust the concentration of oxygen vacancies on the surface of ZnO, and the defective structure of zinc oxide was studied by XRD, XPS, PL, and Raman spectroscopy.

2. Materials and Methods

2.1. Synthesis of Nanocrystalline ZnO and Samples Preparation

Nanocrystalline ZnO was synthesized by decomposition of basic zinc carbonate (Sigma-Aldrich, St. Louis, MO, USA) in air at 300 °C for 24 h according to the following reaction:



The adjustment in the concentration of oxygen vacancies in as-prepared ZnO was achieved by post-annealing of samples (tablets or layers) in He flow (15 mL/min) at 170 °C for 4–12 h. As-prepared nanocrystalline ZnO and post-annealed ZnO are hereinafter referred to everywhere as “ZnO-300” and “ZnO-V_O”, respectively.

2.2. Characterization of ZnO

Phase composition and crystal structure of synthesized zinc oxide was studied by powder X-ray diffraction (XRD) with a Rigaku diffractometer using CuK α radiation (wavelength $\lambda = 1.54059 \text{ \AA}$). Average crystallite size D was calculated using the Sherrer equation:

$$D = \frac{k\lambda}{\beta \cos \Theta} \quad (2)$$

where λ is a wavelength of X-ray radiation, nm; β is a full width at half maximum (FWHM) of a diffraction peak, rad; θ is a diffraction angle; k is a coefficient equal to 0.9. The peak width was previously corrected to take into account instrumental broadening, according to the following equation:

$$\beta = \sqrt{\beta_{exp}^2 - \beta_{app}^2} \quad (3)$$

where β_{exp} is the observed peak width at half height and β_{app} is the instrumental broadening, which was taken equal to 1.57 mrad.

The specific surface area of nanocrystalline ZnO was measured by low-temperature nitrogen adsorption using the BET model with the Chemisorb 2750 instrument (Micromeritics). The average size d_{BET} (μm) of aggregates whose surface is available for gas adsorption was estimated using the equation

$$d_{BET} = \frac{6}{S_{BET} \times \rho} \quad (4)$$

where S_{BET} —specific surface area, m^2/g , ρ —density (5.61 g/cm^3 for ZnO).

X-ray photoelectron spectroscopy (XPS) measurements were performed using a K-Alpha (Thermo Scientific) spectrometer with an Al $K\alpha$ X-ray source ($E = 1486.7\text{ eV}$). The main state of C1s core level was used as a reference with a binding energy (BE) of 285 eV. Morphology of ZnO powders was studied with scanning electron microscope (SEM) Prisma E (Thermo Scientific, Prague, Czech Republic). Samples were preliminary coated with 10 nm layer of gold by Q150R ES plus sputter coater (Quorum Technologies, Laughton, Great Britain).

Photoluminescence was excited with frequency-doubled pulses of a femtosecond titanium–sapphire oscillator (Tsunami, Spectra-Physics, Moscow, Russian Federation) with a central wavelength of 360 nm, repetition rate of 80 MHz, duration of 100 fs, and pulse energy of 10 pJ. After reflecting from a broadband dielectric beamsplitter (Thorlabs, Newton, NJ, USA) mounted at an angle of 45° , femtosecond laser pulses were coupled into an objective lens (Olympus, Tokyo, Japan, $20\times$, 0.5 NA) and focused on the sample. Luminescence signal was collected with the same objective lens and coupled to a monochromator (Acton SP300i, Acton Research Corporation, Acton, MA, USA). Luminescence emission spectra were recorded with an EM-CCD camera (PI MAX 2, Princeton Instruments, Trenton, NJ, USA) installed at the monochromator output. While emission spectra were recorded, the objective focal point was scanned across the $100 \times 100\ \mu\text{m}$ sample area using a piezoelectric scanning stage (NT-MDT).

Raman spectra were registered with a SENTERRA Raman microscope-spectrometer (Bruker, Billerica, MA, USA) using a $50\times$ 0.75 NA microscope objective lens and laser excitation at 785 nm.

2.3. Gas-Sensing Measurements

For sensor measurements, the chips were used consisting of an Al_2O_3 plate $1.5 \times 1.5\text{ mm}$ in size, equipped with platinum contacts with a gap of $200\ \mu\text{m}$ between them (Figure 1a). A platinum electric heater was applied on the reverse side of the plate (not shown in the figure). Nanocrystalline ZnO powder was mixed with α -terpeniol to form a thick paste, which was applied to the measuring plate; then the obtained layer was slowly dried at $50\text{ }^\circ\text{C}$ and then sintered at $300\text{ }^\circ\text{C}$ in air for 24 h to form the ZnO layer of $\sim 50\ \mu\text{m}$ thickness (Figure 1b). The obtained sensors have a linear current–voltage characteristic at bias up to 4 V (Figure 1c). The thickness of the ZnO film was evaluated from SEM images obtained by tilting the Al_2O_3 plate with ZnO layer by 70° (Figure 1c).

The setup for sensor measurements included a measuring cell; LED power supply and its driver; a gas flow control system connected to the gas sources; laboratory-made device for measuring the resistance of sensors using a two-wire method and controlling their temperature. The sensor resistance is measured by applying a constant voltage of 4 V. Synchronization of the operation of electronic devices was carried out under the control of a personal computer (Figure 2).

The PTFE measuring cell was cylindrical and had a volume of 50 mL; an LED was placed in the upper part of the cell, and sensors were located in the lower part, at a distance of 3–4 cm from the LED. The resulting NO_2 gas concentration was obtained by mixing the attested gas mixture ($100 \pm 1\text{ ppm NO}_2$ in N_2) and the synthetic dry air using Bronkhorst mass-flow controllers (Bronkhorst High-Tech B.V., Ruurlo, The Netherlands). During the measurements, the gas flow through the cell was maintained at 100 mL/min . The temperature of sensors during the gas-sensing measurements was maintained with an accuracy of $\pm 2\text{ }^\circ\text{C}$. The UV LED with a peak wavelength at 370 nm was used for photoactivation (Figure 3). The sensor signal to NO_2 was calculated using the equation

$$S = \frac{R_{gas}}{R_{air}} \quad (5)$$

where R_{gas} —resistance of the sensor at the presence of NO_2 ; R_{air} —resistance of the sensor in dry air.

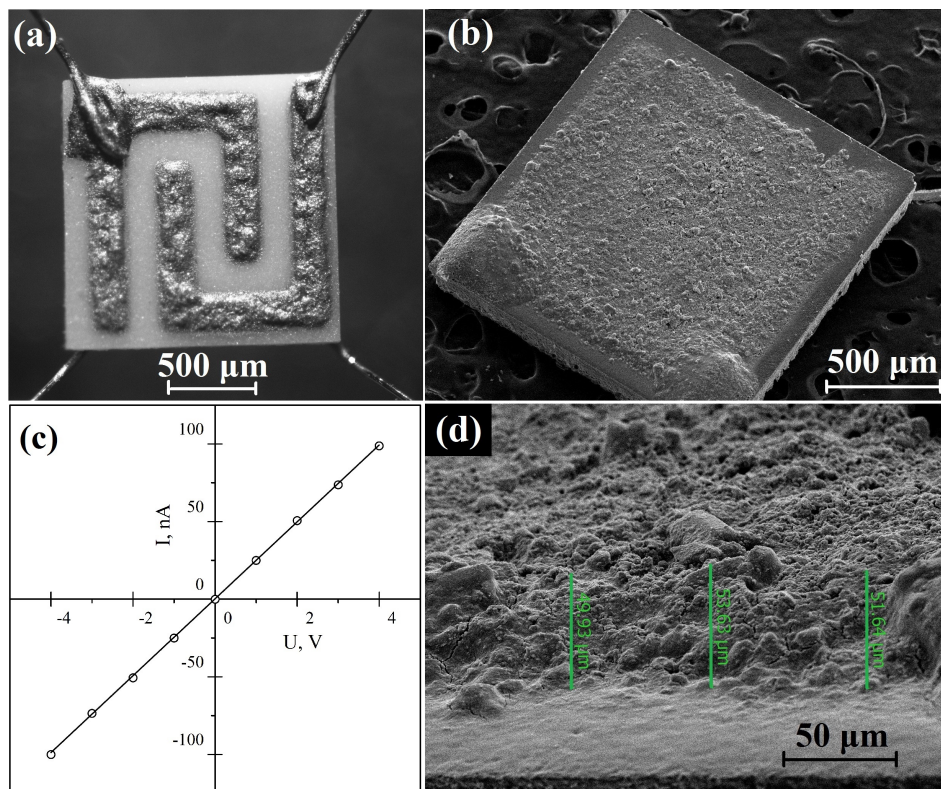


Figure 1. (a) Al₂O₃ measuring plate equipped with two platinum electrodes for measuring the resistance of the sensor layer (image from an optical microscope); (b) SEM image of a measuring plate with an applied ZnO layer; (c) current–voltage characteristic of ZnO sensor measured at 100 °C in the dark; (d) evaluation of the thickness of the applied ZnO layer (SEM image).

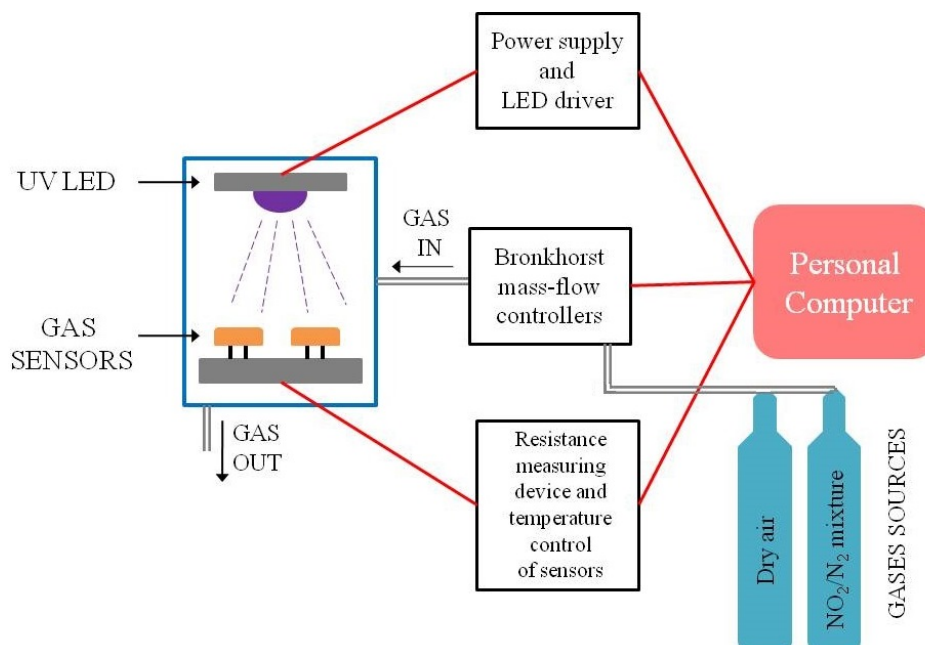


Figure 2. Block representation of the setup for sensor measurements.

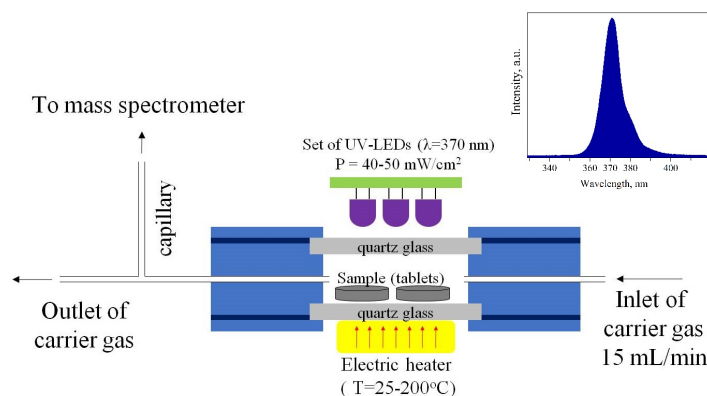


Figure 3. The design of the cell used for photostimulated MS experiments. The inset shows the emission spectrum of the LEDs used for irradiation.

2.4. In Situ Photostimulated Mass Spectrometry

The cell for the MS studies consists of a PTFE frame sealed at the top and bottom with quartz windows 1.5 mm thick (Figure 3). The samples were placed inside the cell on the bottom glass, and irradiation was carried out through the top glass with a set of light-emitting UV diodes. The internal volume of the cell was 15 mL. The electric heater was located under the bottom glass and allowed to heated the samples up to 170 °C in a controlled manner. The cell is equipped with inlet and outlet openings, the location of which is designed for better mixing of the gas mixture inside the cell (Figure S1). The cell inlet is connected to gas sources through a system of valves and gas flow controllers. The gas flow rate through the cell in all experiments was 15 mL/min. The outlet of the cell is connected to the capillary of the quadrupole mass spectrometer (MS7–200, equipped with RGA–200 analyzer, Stanford Research Systems). Mass spectra were recorded in the range of 4–50 a.m.u. (one scan every 9 s) using an electron multiplier with a gain of 500–1000. All measurements were carried out at ambient pressure in the cell to come near the actual operating conditions of gas sensors. For MS studies, the synthesized ZnO powder was pressed into tablets with a diameter of 20 mm and a thickness of 1 mm at a pressure of 60 kg/cm². For measurements, 4 tablets were usually placed in the cell; thus, the irradiated surface area of the samples was about 12.5 cm².

3. Results

3.1. Crystal Structure, Morphology, and Optical Properties ZnO

The powder diffraction pattern of ZnO obtained by annealing of basic zinc carbonate at 300 °C in air is shown in Figure 4a. All observed reflexes belong to a single phase of wurtzite. The phase composition of ZnO-V_O is the same (Figure 4b), and the change in the unit cell parameters is within the measurement error (Table 1). The average crystallite size calculated by Equation (2) for planes (100), (101), and (110) lies in the range of 12–16 nm, while for the plane (002) this size is somewhat larger (Table 1), which may indicate the anisotropic shape of nanocrystals, elongated along the *c* axis [38]. It can also be noted that the calculated average crystallite size of the ZnO-V_O sample is slightly (by 1 nm) smaller than for the ZnO-300 in all crystallographic directions.

Table 1. Crystal lattice parameters and average size of crystal regions in different crystallographic directions of ZnO-300 and ZnO-V_O samples.

Sample	<i>a</i> , nm	<i>c</i> , nm	<i>D</i> ₁₀₀ , nm	<i>D</i> ₀₀₂ , nm	<i>D</i> ₁₀₁ , nm	<i>D</i> ₁₁₀ , nm
ZnO-300	3.2511 (14)	5.2116 (21)	17	20	15	13
ZnO-V _O	3.2518 (12)	5.2133 (18)	16	19	14	12

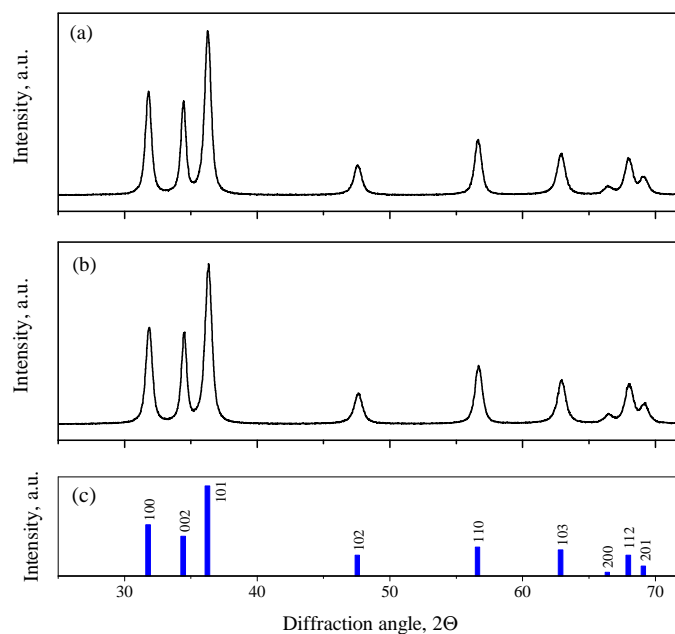


Figure 4. XRD patterns of ZnO-300 (a) and ZnO-V_O (b) powder samples; (c) bar diffractogram of wurtzite ZnO (ICDD # 98-002-9272).

According to the images obtained by SEM, the synthesized ZnO powder consists of micrometer-sized aggregates that are formed from nanoparticles of various morphologies (Figure 5). Higher-resolution images made it possible to establish that the ZnO aggregates are mainly composed of needle-shaped nanoparticles 15–30 nm thick and 170–220 nm long. Similar gas-sensitive ZnO structures were previously obtained in [39] by using the hydrothermal method.

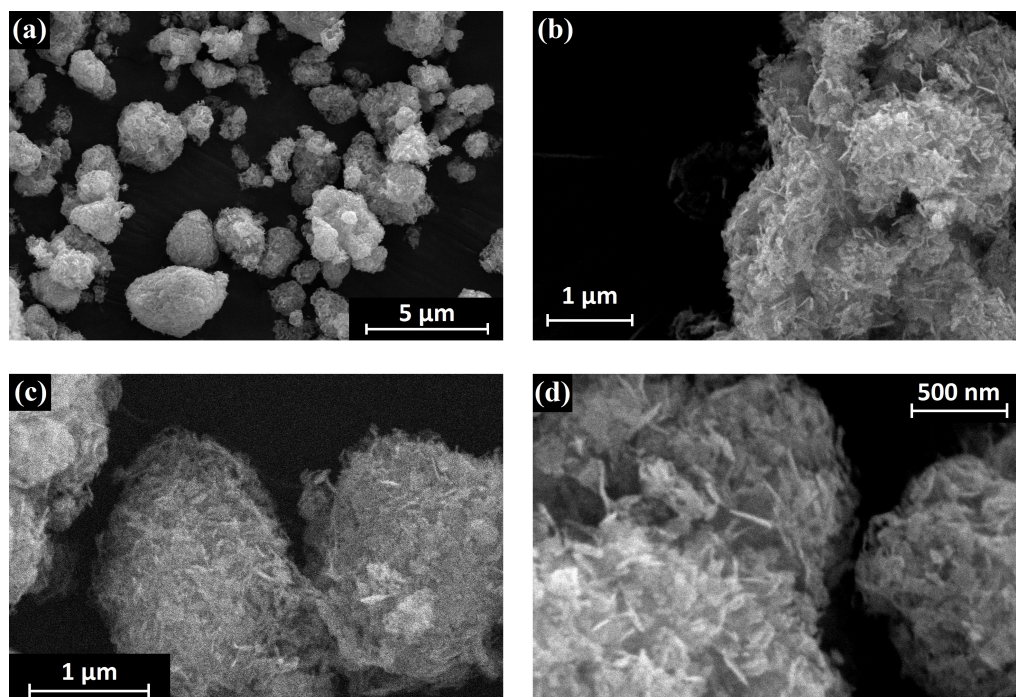


Figure 5. SEM images of synthesized nanocrystalline ZnO powder at different magnifications: (a)—micrometer-sized aggregates; (b–d)—needle-shaped ZnO nanoparticles in aggregates.

The specific surface area of the synthesized ZnO powder was $4.5 \pm 0.5 \text{ m}^2/\text{g}$. Evaluation of the average size of aggregates according to Equation (4) gives an average aggregate size of the order of $0.3 \mu\text{m}$, which is usually smaller than the sizes of aggregates observed in SEM images. This discrepancy can be explained by the porosity of the formed aggregates.

The state of oxygen on the ZnO surface was investigated by XPS. In both ZnO-300 and ZnO- V_{O} samples, the oxygen atoms are represented by at least three charge states (Figure 6). O1s(I) state, with the lowest BE and highest intensity, refers to O^{2-} ions in the ZnO crystal lattice; O1s(II) state, with a BE = 531.2 eV, can be assigned to oxygen ions located near oxygen vacancies [40]; O1s(III) state can appear due to the presence of OH-groups and chemisorbed oxygen on the ZnO surface [20]. The overall Zn:O ratio shows a superstoichiometric oxygen content for both ZnO-300 (1:1.22) and ZnO- V_{O} (1:1.17) samples. The BEs of O1s charge states in the samples, as well as their relative content, are listed in Table 2.

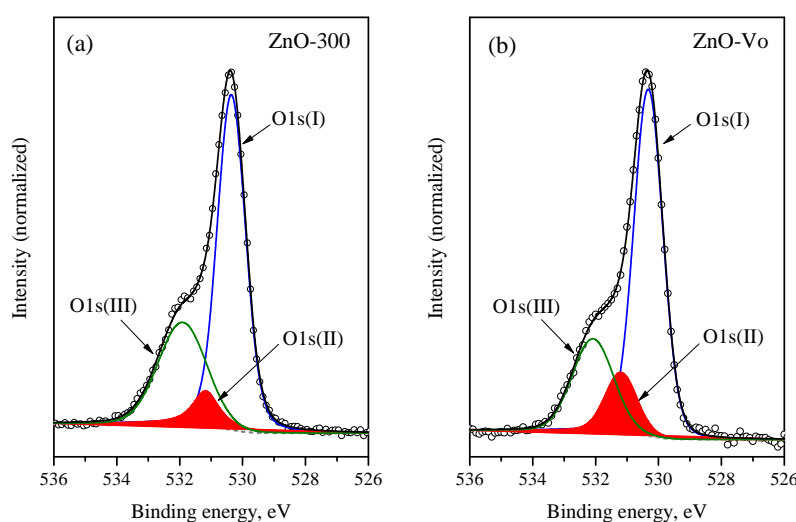


Figure 6. XP-spectra of ZnO-300 (a) and ZnO- V_{O} (b) samples in the O1s region.

Table 2. BE positions and relative content of O atoms in different charge states in ZnO-300 and ZnO- V_{O} samples.

Sample	BE Position, eV			Content, at. %		
	O1s(I)	O1s(II)	O1s(III)	O1s(I)	O1s(II)	O1s(III)
ZnO-300	530.4	531.2	532.0	61.7	7.8	30.5
ZnO- V_{O}	530.3	531.2	532.0	64.2	12.4	23.4

The PL spectra of ZnO-300 and ZnO- V_{O} samples are shown in Figure 7a. Generally, both samples exhibit near-band emission peak with maximum of around 390 nm and broad defect band emission centered around 590 nm. When the spectra are normalized to the near-band emission peak, it can be seen that the defect emission intensity decreases after ZnO annealing in an inert atmosphere.

The Raman spectra of the synthesized ZnO-300 and ZnO- V_{O} powders are shown in the range of $100\text{--}600 \text{ cm}^{-1}$ in Figure 7b. They represent typical ZnO wurtzite spectra. Both spectra show intense peaks corresponding to the $E_2(\text{high})$ (438 cm^{-1}) and $E_2(\text{high}) - E_2(\text{low})$ (331 cm^{-1}) modes, and less intense modes $A_1(\text{TO})$, $E_1(\text{TO})$, and $2E_2(\text{low})$. There is no significant shift between the peaks of both samples; however, as a result of post-annealing in an inert atmosphere, the $E_2(\text{high})$ line intensity decreases by more than two times, and the FWHM increases from 9 to 14 cm^{-1} . A decrease in the intensity of the peak and an increase in its width indicate the disordering of the crystal structure near the surface of the ZnO grains.

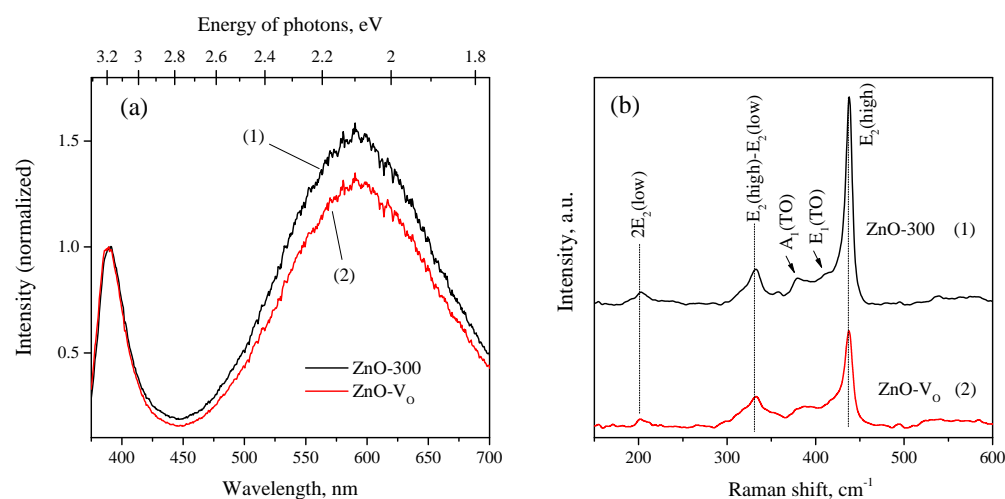


Figure 7. (a) Normalized PL spectra of ZnO-300 (1) and ZnO-V_O (2) samples at RT (excitation wavelength 360 nm); (b) Raman spectra of ZnO-300 (1) and ZnO-V_O (2) samples at RT (excitation wavelength 785 nm).

3.2. Photostimulated Oxygen Adsorption on ZnO

Photostimulated oxygen-related processes were studied using high-purity helium (residual oxygen content of about 0.15 ppm) as carrier gas. In order to achieve a steady state, a He gas was preliminary passed for several hours through the cell with ZnO tablets in dark. Figure 8 shows the mass spectrum in the range of 11–48 a.m.u. of carrier gas passing through the cell with ZnO tablets under stationary dark conditions (black line). The spectrum shows residual impurities including H₂O vapor, O₂, N₂, Ar, and CO₂, which are present at concentrations of less than 1 ppm. When the samples are irradiated with UV light through the quartz window of the cell (Figure 3), a noticeable decrease in the oxygen concentration in the carrier gas is registered (Figure 8). The absorption of oxygen from the carrier gas in this experiment indicates its photoadsorption, which occurs under UV radiation.

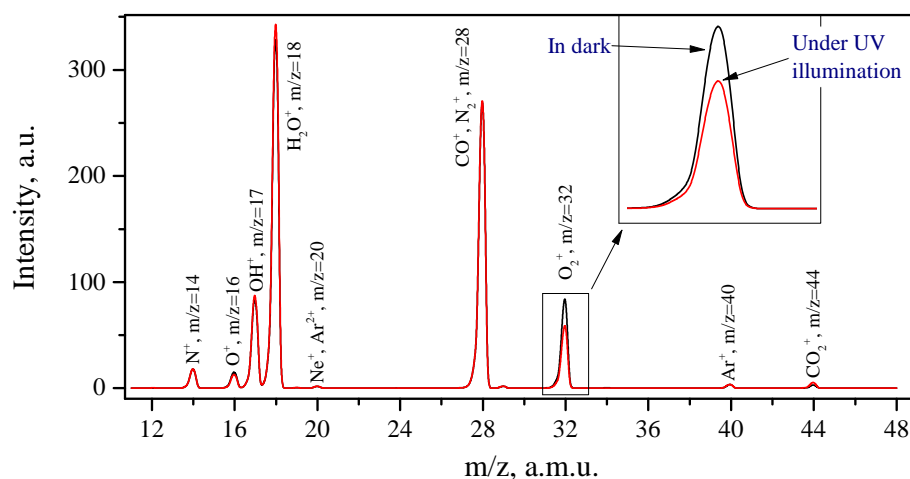


Figure 8. Mass spectrum of the carrier gas leaving the cell with loaded ZnO tablets under stationary dark conditions (black line) and after 9 min of turning on UV radiation (red line).

Next, the oxygen concentration in the carrier gas was continuously monitored by the ion current with $m/z = 32$ under the UV light illumination ($\lambda_{max} = 370$ nm) in the temperature range of 31–150 °C (Figure 9). The kinetics of changes in oxygen concentration under UV light include a sharp decline at the initial time period and a slow increase during illumination, which is determined by the kinetic parameters of the photoadsorption process.

When the UV illumination is turned off, the oxygen concentration is quickly recovered to its residual level. This behavior indicates the process of irreversible photoadsorption. With a stepwise increase in the temperature of the ZnO-300 tablets to 50, 100, and 150 °C, an O₂ photoadsorption under UV radiation remains and is gradually enhanced with increasing temperature.

Reductive post-annealing of the ZnO-300 tablets was carried out directly in the MS cell in a He flow at 170 °C for 12 h, after which samples were also cooled down to RT in an inert atmosphere. As can be seen in Figure 9, the resulting ZnO-V_O sample also demonstrates the effect of irreversible photoadsorption of oxygen in the temperature range from RT to 150 °C; however, photoadsorption is enhanced by 5–6 times at RT compared to the ZnO-300 sample. At the same time, the effect of temperature on the O₂ photoadsorption is weakly expressed and consists of a slight decrease in photoadsorption upon heating to 150 °C.

Thus, it can be concluded that for the synthesized ZnO annealed in air, as well as for the ZnO after a reductive post-annealing in an inert atmosphere, photoadsorption of oxygen under UV radiation is typical. At the same time, the ZnO-V_O sample demonstrates enhanced photoadsorption compared to the ZnO-300 sample.

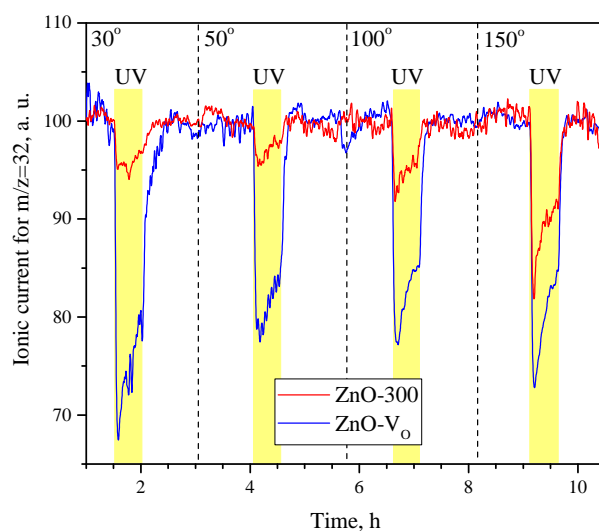


Figure 9. Comparative baseline-corrected graphics showing photoadsorption of oxygen from carrier gas on ZnO-300 (1) and ZnO-V_O (2) tablets under UV light illumination (370 nm) in the temperature range of 30–150 °C, determined from the ion current by $m/z = 32$.

3.3. Photostimulated NO₂ Processes on the ZnO Surface

3.3.1. Photoadsorption NO₂ from Oxygen-Depleted Atmosphere

Photostimulated processes on the ZnO surface involving NO₂ molecules were firstly studied in oxygen-depleted gas atmosphere using a gas mixture based on high-purity He, containing 100 ppm NO₂ and 0.15 ppm O₂, as a carrier gas. To establish the effect of UV light on the adsorption equilibrium between gaseous and chemisorbed forms of NO₂, the experiment was designed as follows: a carrier gas was passed through the cell with samples under dark conditions at RT for 2 h to achieve the steady state; then the UV light was turned on for a period of 60 min. The effect of UV irradiation was then tested at 31 °C, 50 °C, 100 °C, and again at 31 °C. Concentration of NO₂ and O₂ in the carrier gas was monitored by changing the ion current for ions with $m/z = 30$ and 32 a.m.u., respectively. Mass 30 a.m.u. was chosen to monitor the NO₂ concentration, because this mass corresponds to NO⁺ ions, which is the most intense line in the mass spectrum of NO₂, while the intensity of the line with $m/z = 46$ corresponding to NO₂⁺ ions is only 38% of the intensity of the line with $m/z = 30$. As in the previous, measurements on ZnO-300 samples were firstly carried out, then the reductive post-annealing of the new ZnO tablets was performed at 170 °C for 12 h direct in the MS cell.

The results of the MS experiments are summarized in Figure 10. As can be seen, post-treatment of the ZnO sample in an inert atmosphere dramatically changes its reactivity upon interaction with NO_2 under UV-activation.

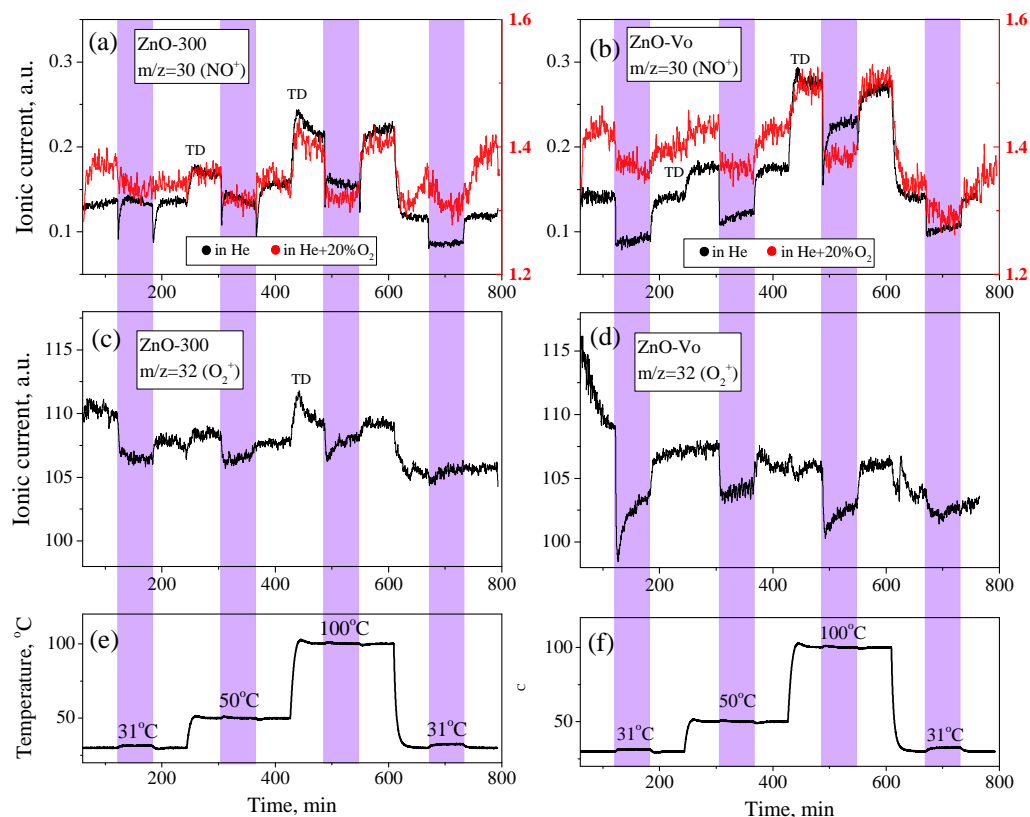


Figure 10. Changes in the ionic current during heating and UV illumination of ZnO tablets obtained from MS: (a) NO_2 ($m/z = 30$) in an atmosphere of He/100 ppm NO_2 (black line) and He/20% O_2 /100 ppm NO_2 (red line) for ZnO-300 sample; (b) NO_2 ($m/z = 30$) in an atmosphere of He/100 ppm NO_2 (black line) and He/20% O_2 /100 ppm NO_2 (red line) for ZnO- V_O sample; (c) O_2 ($m/z = 32$) in the He/100 ppm NO_2 atmosphere for ZnO-300 sample; (d) oxygen ($m/z = 32$) in the He/100 ppm NO_2 atmosphere for ZnO- V_O sample; (e,f) temperature profile of the experiment.

When a freshly annealed in air ZnO sample is irradiated by UV light, a sharp decline in NO_2 concentration is immediately observed, which indicates the photoabsorption of NO_2 from the carrier gas. However, only a sharp single peak of photoadsorption occurs, after which the NO_2 concentration in the carrier gas quickly recovers to the initial level and remains close to this level during the entire illumination period. After turning off the UV light, again a single NO_2 adsorption peak is observed. This behavior looks curious, since if the photoadsorption occurs under the light radiation, then when the light is turned off, one can expect the desorption of excess adsorbed molecules, or at least no change in their concentration in gas phase, if photoadsorption was irreversible. Instead, additional adsorption effect is seen when the UV is turned off. The appearance of sharp adsorption peaks after the turning on and off of UV light is characteristic of ZnO samples annealed in an oxygen-rich atmosphere and will be referred to below as “turn-on”- and “turn-off”-induced peaks.

Heating ZnO tablets up to 50 °C in the dark in He/ NO_2 flow leads at first to an increase in the NO_2 concentration in the carrier gas due to thermally activated desorption (TD) of chemisorbed NO_2 molecules from ZnO surface. Exposure to UV illumination, as in the previous case, leads to the appearance of sharp “turn-on”- and “turn-off”-induced adsorption peaks; however, along with fast photoadsorption processes, slow photoadsorp-

tion occurs, which consists of a decrease in the NO₂ concentration in the carrier gas during the entire illumination period.

A similar picture is observed when the ZnO tablets are heated up to 100 °C. First, TD of NO₂ is observed, and after the establishment of the baseline, the effect of UV illumination leads to fast and slow processes of NO₂ photoadsorption. Generally, as the temperature increases, the following trends are noted: fast “turn-on”- and “turn-off”-induced peaks become less distinct, while the rate of “slow” photoadsorption, i.e., the drop in NO₂ concentration in the carrier gas during the irradiation period, increases.

After cooling to room temperature, the ZnO samples exhibit a fundamentally different behavior towards NO₂ compared to the sample before heating: fast NO₂ adsorption peaks disappear and slow step-shaped photoadsorption is clearly observed. This indicates that the surface of the sample has changed during the experiment. Slow photoadsorption was also irreversible, i.e., no desorption of NO₂ was registered after turning off the UV light.

Along with NO₂ photoadsorption during UV irradiation, O₂ photoadsorption was observed on the ZnO surface. The kinetics of O₂ photoadsorption are devoid of fast peaks as per those observed in the photoadsorption of NO₂, and were “slow”, although the effect of temperature on the photoadsorption kinetics is noticeable. In addition to that of NO₂, TD of O₂ is observed when heated to 50 and 100 °C. After the sample is cooled, oxygen photoadsorption is observed in a very weak form compared to the state before heating.

The next experiment was carried out on new ZnO tablets which were post-annealed directly in the measuring cell at 170 °C in a He flow for 12 h. After cooling the sample to room temperature and passing mixture He/NO₂ until a dark baseline was established, the sample was irradiated for 1 h with UV light. As a result, the sample exhibits step-like irreversible photoadsorption of NO₂ from the carrier gas, with no fast adsorption peaks.

When heated to 50 °C, TD of NO₂ occurs, against which a similar pattern of slow step-shaped photoadsorption of NO₂ is also observed under UV irradiation. At a temperature of 100 °C, another TD peak of NO₂ is observed; however, NO₂ photoadsorption is characterized by both fast peaks and slow photoadsorption, which, in this case, does not have a step-like shape, but is characterized by kinetics, according to which the photoadsorption rate decreases exponentially during the illumination period.

After cooling the ZnO-V_O tablets to RT, they show a similar NO₂ photoadsorption behavior compared to the state before heating, indicating that the sample has not changed during the MS measurements.

NO₂ photoadsorption, as in the previous case, is accompanied by O₂ photoadsorption, the behavior of which is nonmonotonous. At room temperature, a significant increase in O₂ photoadsorption is seen (compared to the ZnO-300 sample). Then, at 50 °C, the photoadsorption rate decreases, and at 100 °C, it increases again. After the measurement cycle, at room temperature, NO₂ photoadsorption is weaker than before measurements.

3.3.2. Photoadsorption NO₂ from Oxygen-Rich Atmosphere

Since semiconductor sensors are usually aimed to operate in ambient atmosphere, it is of practical interest to study photostimulated processes in an environment with a high oxygen content. In addition, this will make it possible to more clearly understand the role of oxygen in the photostimulated processes when comparing the results of experiments in oxygen-depleted and oxygen-rich atmospheres.

For the abovementioned purposes, a carrier gas based on high-purity He containing 100 ppm NO₂ and 20% oxygen was used. Since the content of NO₂ and O₂ differed by more than six orders of magnitude, their simultaneous determination by MS is difficult, and only the change in NO₂ concentration was registered. The results of NO₂ photoadsorption under UV radiation in oxygen-rich atmosphere on ZnO-300 and ZnO-V_O are also shown in Figure 10a,b, respectively (red lines).

From the data obtained, it can be seen that NO₂ photoadsorption for both samples is typical, where rate increases with increasing of temperature. In this case, the characteristic

“turn-on”- and “turn-off”-induced peaks previously observed in an inert atmosphere are absent. Photoadsorption on samples measured at RT before and after heating is reproducible.

However, the relative drop in NO₂ concentration during photoadsorption from an oxygen-depleted and oxygen-rich atmosphere for the samples is significantly different. Thus, for ZnO-300 sample at 50 °C, during photoadsorption from He/NO₂ atmosphere, the average drop in the ion current for $m/z = 30$ is 14%, while from a He/O₂/NO₂ atmosphere, it is only 4%. The same trend is noted for ZnO-V_O sample: during NO₂ photoadsorption from a He/NO₂ atmosphere, the average drop in the ion current for $m/z = 30$ is 34%, while from a He/O₂/NO₂ atmosphere, it is 5%. Thus, in both oxygen-depleted and oxygen-rich atmospheres, for nanocrystalline ZnO, the photoadsorption of NO₂ under UV radiation is typical, while the high content of oxygen hinders the photoadsorption of NO₂; as a result, the rate of photoadsorption is decreased by 3–7 times.

3.4. UV-Activated Gas Sensitivity ZnO to NO₂

The gas sensitivity of the synthesized nanocrystalline ZnO was studied for NO₂ in the concentration range of 0.5–5.8 ppm in the temperature range of 30–100 °C in dark and under continuous UV illumination (370 nm) (Figure 11). The dark resistance of ZnO-300 and ZnO-V_O samples at room temperature was around $2 \cdot 10^{10}$ and $5 \cdot 10^{10}$ Ω, respectively. At RT in dark, a response to 0.5 and 1.0 ppm of NO₂ is observed; however, in the presence of >1.9 ppm NO₂, the resistance of both sensors irreversibly moves off scale ($R > 10^{11}$ Ω). At 50 °C, the dark resistance of the sensors slightly decreases to $\sim 5 \cdot 10^{10}$ Ω and the sensor response is observed in the range of 0.5–5.8 ppm; however, the sensor signal cannot be reliably calculated due to the fact that the resistance of the sensors moves off scale at a NO₂ concentration of more than 1.9 ppm. At 100 °C, the dark resistance of the sensors decreases even more to 10^9 Ω, and the sensor response is observed in the entire range of 0.5–5.8 ppm of NO₂. The dependence of the sensor signal on the NO₂ concentration in the dark at 100 °C is shown in Figure 12 for both samples.

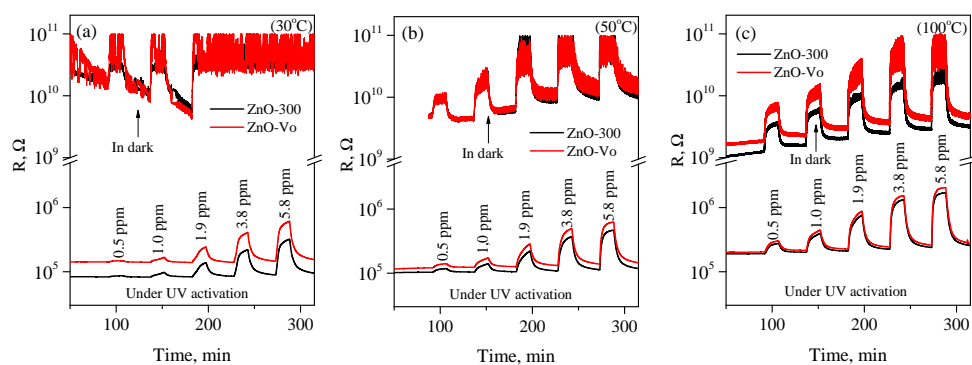


Figure 11. Gas-sensing measurements for ZnO-300 and ZnO-V_O samples for NO₂ in dark and under UV activation at 30 °C (a), 50 °C (b), and 100 °C (c).

Under UV illumination, the steady-state resistance of ZnO-300 and ZnO-V_O sensors at 30 °C in air decreased to $8.5 \cdot 10^4$ and $1.4 \cdot 10^5$ Ω, respectively, as a result of photoconductivity (Figure 11). The observed photoconductivity in nanocrystalline ZnO arises due to the excitation of electrons from the valence band and local levels near the top of the valence band into the conduction band of ZnO [41,42]. In the presence of NO₂, both samples increase resistance, which reversibly recovers to the baseline value in air in the absence of NO₂. It can be seen that both samples in this range demonstrate a reversible sensor response to NO₂, which increases with increasing NO₂ concentration. Figure 12 shows the dependencies of the sensor signal of both samples calculated using Equation (5), from which it follows that in a given NO₂ concentration range, the dependence is close to linear on the log–log plot. Sensor signal of ZnO-V_O sensor is always higher than ZnO-300 at equal temperatures; for example, at 30 °C and 3.8 ppm NO₂, sensor signal increases by 10% for ZnO-V_O compared to ZnO-300. An increase in temperature leads to an increase in the

sensor signal of both samples. With a simultaneous increase in both concentration and temperature, the difference in the sensor response of the samples becomes more pronounced.

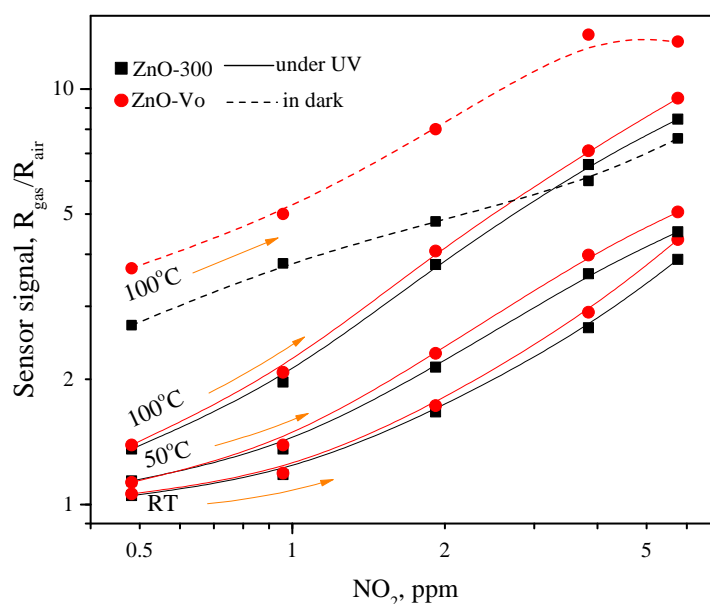


Figure 12. The concentration dependence of the sensor signal to NO_2 for ZnO-300 (rounds) and ZnO- V_O (squares) sensors, measured under UV irradiation at temperatures of 30 °C, 50 °C, and 100 °C (solid lines) and under dark conditions at 100 °C (dashed line).

4. Discussion

4.1. Defect Structure of Synthesized Nanocrystalline ZnO

Synthesized nanocrystalline ZnO showed a remarkable change in reactivity after annealing in an inert atmosphere, which can be associated with a change in the defective structure of its surface. Due to the relatively low synthesis temperature, as well as the high degree of rearrangement of the crystal structure as a result of the reaction (1), the formation of a highly defective ZnO structure is expected, in which atoms do not completely occupy the crystal lattice sites, and the formation of interstitial defects and vacancies is very likely. The defect structure of ZnO and the effect of post-annealing on it can be assumed from the results of XPS and PL studies (Figures 6 and 7a).

The XPS analysis demonstrates that the intensity of O1s(II) charge state, which can be assigned to O atoms near oxygen vacancies, increases from 7.8 to 12.4%; more than 1.5 times for ZnO-300 sample compared to ZnO- V_O sample (Table 2). This is consistent with the assumption that ZnO annealing in an inert atmosphere leads to an increase in the concentration of oxygen vacancies on the surface due to a decrease in the partial pressure of oxygen in the system:



Thus, the number of oxygen atoms neighboring with V_O also increases, which leads to an increase in the signal intensity of O1s(II).

On the other hand, the position of the observed defective PL band can, rather, be attributed to the process of electron recombination at interstitial oxygen atoms [43–45]. Thus, Chandrinou et al. reported on the synthesis of ZnO nanorods and showed that the intensity of the defective luminescence band observed at 580 nm increases with an increase in the oxygen concentration in the atmosphere where post-annealing or synthesis of ZnO nanorods took place [46]. In Figure 7a, we also observe a decrease in the intensity of the

defective PL band of ZnO after post-annealing in an inert gas, which can be associated with a decrease in the concentration of interstitial oxygen:



At the same time, it should be noted that the observed defect PL band is very wide and most likely consists of several peaks; therefore, it is difficult to recognize in it the lines corresponding to V_O -related luminescence.

The presence of interstitial oxygen in the ZnO can also be revealed from the XP-spectra. Assuming that an interstitial oxygen atom relaxes into a split-interstitial configuration in which it shares a lattice site with one of the nearest-neighbor substitutional oxygen atoms (with a distance of O-O 1.46 Å) [45], forming a chemical bond with the Zn atom, the corresponding O1s peak is expected to have a BE slightly higher than that for lattice oxygen in ZnO. Drawing an analogy with ZnO_2 , which has an O–O binding and a BE = 532.8 eV for O1s, it is observed [47] that the charge state of O_i atoms in synthesized needle-shaped nanocrystalline ZnO can be assigned to state O1s(III). This assumption correlates with a decrease in the intensity of O1s(III) state in ZnO after post-annealing (Table 2).

Formation of oxygen vacancies on the ZnO surface as a result of post-annealing in an inert atmosphere can be assumed due to decrease in the size of coherent scattering region in comparison with the ZnO-300 sample (Table 1). Apparently, this effect can be attributed to the broadening of X-ray reflections due to increased disordering of the near-surface region of ZnO crystallites during the formation of oxygen vacancies, so the size of coherent scattering region becomes smaller than the grain size.

Oxygen vacancies can ionize, donating electrons to the conduction band:



According to calculations given in [48], in ZnO the existence of oxygen vacancies in the neutral V_O and doubly positively charged V_O^{2+} form is most probable, while singly charged vacancies V_O^+ are not stable.

For ZnO- V_O , formation of neutral vacancies is supported by the fact that there was no decrease in the electrical resistance compared to the ZnO-300 sample both in the dark and under UV light (Figure 11).

4.2. Surface Reactivity of ZnO under UV Activation

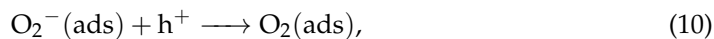
4.2.1. Oxygen Photoadsorption

Photostimulated processes involving oxygen on the surface of ZnO were previously studied by various experimental methods [49–51]. Titov et al. also observed irreversible photoadsorption of oxygen on the ZnO surface by in situ MS under UV radiation [52,53]. The spectroscopic data given in work [54] indicate the formation of chemisorbed oxygen on the surface of metal oxides in a singly charged form up to a temperature of 150 °C, while the formation of other charge forms of chemisorbed oxygen is not confirmed.

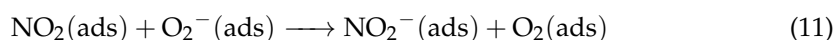
In this work, the temperature dependence of the oxygen photoadsorption on ZnO was also studied (Figure 9). It should be taken into account, firstly, that the increase in the rate of oxygen adsorption on the ZnO-300 sample with increasing of temperature can be attributed to its gradual reducing in an inert carrier gas. Thus, the study of the temperature dependence of the photoadsorption properties of the “oxidized” ZnO in an inert atmosphere is not indicative. The temperature dependence of the O_2 photoadsorption rate on the ZnO- V_O is weakly expressed. Maximum photoadsorption rate is achieved at room temperature, then, when heated to 150 °C, it gradually decreases (Figure 9). Generally, we have shown that photoadsorption on the surface of a nanocrystalline ZnO can be enhanced by reductive post-annealing in an inert gas by 5–7 times. Using a combination of

physicochemical methods, it is assumed that the enhancement of photoadsorption may be associated with an increase in the surface concentration of oxygen vacancies.

Despite the fact that reactions of chemisorbed oxygen with photogenerated holes,



are often reported in the literature, we did not observe photodesorption of oxygen in a He flow for either ZnO-300 and ZnO-V_O samples in the temperature range of 30–150 °C. Although the behavior of oxygen in the presence of NO₂ is less clear (Figure 10), only photoadsorption is also registered for both ZnO-300 and ZnO-V_O samples, which calls into question photoactivated reactions of the following type:



which imply the displacement of part of the chemisorbed oxygen molecules from the surface of the ZnO by photosorbing NO₂ molecules.

4.2.2. NO₂ Photoadsorption

MS study of the photostimulated processes of NO₂ on the ZnO surface, to the best of our knowledge, was carried out for the first time. The mass conservation law for processes occurring in an MS cell can be written as follows:

$$(C_{in} - C_{out}) \times \frac{\Delta V}{\Delta t} \frac{1}{V_m^T} = \left(\frac{\Delta n(\text{ads})}{\Delta t} \right)_{\text{dark}} + \left(\frac{\Delta n(\text{ads})}{\Delta t} \right)_{\text{ph}} \quad (12)$$

where C_{in} —initial concentration of NO₂ in the carrier gas, volume fraction, ppm; C_{out} —residual concentration of NO₂ in the carrier gas at the outlet of the cell, volume fraction, ppm; V_m^T —molar volume, mL/mol at operating temperature T , K; $\Delta V/\Delta t$ —the flow rate mL/min; $(\Delta n(\text{ads})/\Delta t)_{\text{dark}}$ —NO₂ adsorption rate in dark, mol/min; $(\Delta n(\text{ads})/\Delta t)_{\text{ph}}$ —NO₂ photoadsorption rate, mol/min. Equation (12) is exactly true when the temperatures of the incoming and outgoing flows are equal. When the cell is heated, the flow rate increases due to volumetric expansion, which leads to a decrease in the NO₂ concentration in the carrier gas. However, the exact temperature of the gas flow reaching the mass spectrometer is difficult to calculate due to unknown heat losses, and the temperature of the capillary of the mass spectrometer varies in the range of 40–70 °C, so the steady-state $C_{in} - C_{out}$ expression at different temperatures must be estimated experimentally.

Under dark conditions, the photoadsorption rate is zero, and the change in the NO₂ concentration at the outlet of the cell is determined only by the adsorption rate. The quasi-stationary state corresponding to $C_{in} - C_{out} = \text{const}$ condition is achieved by establishing a stationary adsorption rate $(\Delta n(\text{ads})/\Delta t)_{\text{dark}} = \text{const}$, which is a function of C_{in} , temperature, and flow rate. Under UV irradiation, photoadsorption occurs and the rate of absorption of NO₂ from the carrier gas increases relative to the quasi-equilibrium dark value, as a result of which C_{out} decreases from the steady-state value. The deviation of the residual NO₂ concentration due to UV irradiation C'_{out} from the dark stable value C_{out} can be written as $\Delta C(\text{ph}) = C_{out} - C'_{out}$, respectively, the photoadsorption rate in terms of experimentally determined quantities is expressed as $\Delta C(\text{ph}) \times \Delta V/\Delta t$.

According to the data obtained, active NO₂ adsorption on ZnO also occurs in dark conditions: at $C_{in} = 100$ ppm, a residual concentration $C_{out} = 4$ ppm of NO₂ at 30 °C is registered (see calibration graph, Figure S2); thus, most of the NO₂ molecules entering the cell are adsorbed on the ZnO surface. Exposure to UV light in the case of sample ZnO-V_O, for example, results in C'_{out} to about 1 ppm at 31 °C, i.e., $\Delta C(\text{ph}) = 3$ ppm (Figure 9).

The photoadsorption rate of NO₂ on ZnO is significantly affected by the presence of oxygen: when using a carrier gas with 20% oxygen, the residual NO₂ concentration C_{out} is about 46 ppm (at 30 °C) (Figure 9). Exposure of ZnO to UV light in an oxygen-rich atmosphere also leads to an increase in the NO₂ photoadsorption rate, but to a much lesser extent than in oxygen-depleted atmosphere. Thus, for sample ZnO-V_O, irradiation with

UV light leads to C'_{out} to about 44 ppm at 31 °C, i.e., $\Delta C(ph) = 2$ ppm. Thus, the presence of oxygen significantly hinders the process of NO₂ adsorption on the ZnO; in this case, the relative rate of photoadsorption also decreases. This conclusion can be supported by the results of [55], where authors showed that the sensor signal and the sensitivity of the ZnO sensor to NO₂ are much higher in a N₂ atmosphere than in air.

It is interesting to reveal the reasons for the change in the ZnO reactivity due to its post-annealing in an inert atmosphere. Some suggestions can be proposed:

- (i) When a ZnO sample is annealed in an inert atmosphere, the surface can be reduced with the formation of oxygen vacancies, as a result of which an increase in the surface concentration of oxygen vacancies leads to a change in surface reactivity.
- (ii) When ZnO is heated in an inert gas flow, the surface of ZnO is cleaned as a result of thermal desorption of H₂O, CO₂ (Figure S3), and other volatile contaminants, as well as chemisorbed oxygen; existing adsorption sites suitable for NO₂ adsorption become unoccupied and this increases the reactivity of the surface.

To verify whether surface cleaning really affects the reactivity of the ZnO when interacting with NO₂ under UV radiation, an additional experiment was carried out in which the post-annealing of the as-prepared ZnO was carried out in an oxygen-rich atmosphere (He + 20% O₂) at 170 °C for 12 h, and after that, the NO₂ photoadsorption from He + 100 ppm NO₂ mixture was studied at RT. In an oxygen-rich atmosphere, the reduction of the ZnO surface with the formation of vacancies is excluded, while the removal of water, CO₂, and other volatile contaminants also occurs. It can be seen from Figure 13a that the photoadsorption properties of ZnO post-annealed in an oxygen-rich atmosphere are close to those of the as-prepared ZnO, and the photoadsorption curve contains characteristic “turn-on”- and “turn-off”-induced peaks.

Another assumption may be that the effect of post-annealing in an inert atmosphere on the reactivity of ZnO is due to the removal of chemisorbed oxygen from the surface. To test this hypothesis, a next experiment was carried out in which the ZnO was post-annealed in He flow, after which its NO₂ photoadsorption properties were tested under UV irradiation in He + 100 ppm NO₂ atmosphere. A typical step-like response was obtained as a result, showing active absorption of NO₂ from carrier gas during the illumination (Figure 13b). After that, the ZnO was exposed to an oxygen-rich atmosphere (He + 20% O₂) for 90 min in the dark at RT, and then the NO₂ photoadsorption properties were tested again. As can be seen, the effect of oxygen treatment did not lead to degradation of the photoadsorption properties of the sample (Figure 13c).

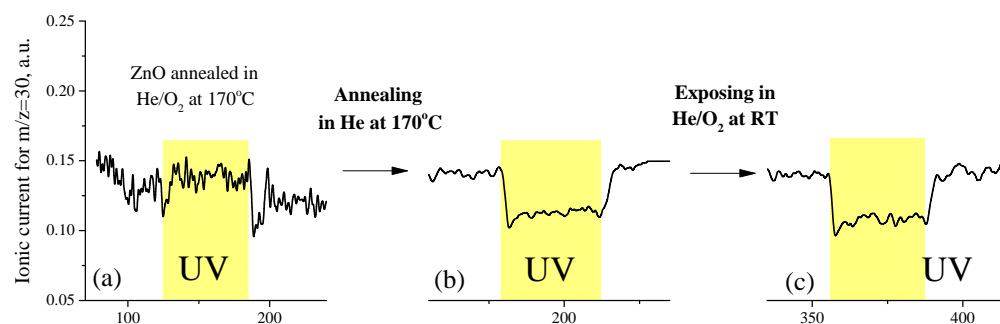


Figure 13. NO₂ photoadsorption experiments on ZnO samples with different treatment history: (a) as-prepared ZnO was post-annealed in (He + 20% O₂) atmosphere at 170 °C for 12 h (arrows show “turn-on”- and “turn-off”-induced photoadsorption peaks); (b) ZnO sample after annealing of the previous sample in He atmosphere at 170 °C for 12 h; (c) ZnO sample after exposing of the previous sample in (He + 20% O₂) atmosphere at RT for 12 h.

From the studies performed, it follows that the enhancement of NO₂ photoadsorption on ZnO after post-annealing in an inert atmosphere is not associated with the effect of

cleaning the surface from O₂, H₂O, CO₂, and other molecules, but is more likely associated with the formation of surface oxygen vacancies. The adsorption of NO₂ and O₂ on the defected ZnO surface was considered by Gaoda [34], and he came to the conclusion that neutral oxygen vacancies are more preferable adsorption sites for O₂ molecules, while doubly charged ones are more preferable for NO₂. In our experiments on the reduced ZnO-V_O, an increase in the photoadsorption of both O₂ and NO₂ was noted.

The kinetics of NO₂ photoadsorption on synthesized ZnO samples demonstrate an atypical form. In general, the adsorption (chemisorption) rate obeys the equation

$$\frac{d\Gamma_{\text{NO}_2}}{dt} = A(1 - \Theta) p_{\text{NO}_2} \Gamma_{\infty} \exp\left(-\frac{E_A}{k_B T}\right) \quad (13)$$

where Γ_{NO_2} is the surface concentration of chemisorbed NO₂, A is a pre-exponential factor, $(1 - \Theta)$ is the fraction of free adsorption centers (V_{O}), p_{NO_2} is pressure of NO₂ in gas phase, Γ_{∞} is total surface concentration of adsorption centers, E_A is adsorption activation energy, and k_B and T are Boltzmann constant and temperature, respectively. As follows from Equation (13), when the adsorption sites are filled, the photoadsorption rate should decrease. Such a picture is observed, for example, in the case of photoadsorption of oxygen on ZnO (Figure 9). However, the kinetics of NO₂ photoadsorption on ZnO have an unusual character, including fast and slow processes.

Fast photoadsorption processes (labeled above as “turn-on”- and “turn-off”-induced peaks) are only characteristic of as-prepared or re-annealed in an oxygen-rich atmosphere ZnO, since the “oxidized” ZnO samples contain a low number of oxygen vacancies, which are the main adsorption sites for NO₂ molecules, and the “turn-on”-induced peaks may occur due to the rapid filling of the remaining oxygen vacancies during NO₂ photoadsorption. A too-fast filling rate does not allow a high-resolution kinetic curve to be obtained (scanning rate is one measurement per 9 s), so only photoadsorption as a single peak is recorded in this case. Adsorption of NO₂ after turning off the UV light indicates that during illumination, a decrease in the equilibrium surface concentration of chemisorbed NO₂ molecules took place. Therefore, under dark conditions, the surface concentration of chemisorbed NO₂ molecules is immediately replenished by absorption from the carrier gas, which appears as a “turn-off”-induced peak on the graph. A decrease in the concentration of chemisorbed NO₂ molecules during illumination period can occur due to their slow photodesorption or their disproportionation reaction, or due to irreversible binding to the ZnO surface with the formation of zinc nitrate.

Another variant of the kinetics of NO₂ photoadsorption on the ZnO surface, which was observed in our experiments, is slow photoadsorption with a characteristic step-like shape on the graph. This was observed for the ZnO-V_O sample in an oxygen-depleted atmosphere and for both the ZnO-300 and ZnO-V_O samples in oxygen-rich atmospheres. This dependence shows that the number of adsorption sites does not decrease in the process of photoadsorption. This may indicate a chemical reaction between NO₂ and ZnO, which follows the photoadsorption process.

Based on the data presented in Figure 10a,b, the temperature dependence of the rate of NO₂ photoadsorption on the ZnO from the oxygen-rich carrier gas can be analyzed. Taking the $\Delta C(ph)$ values extracted from graphs in Figure 10a,b, and irradiated surface area (12.5 cm²), the specific rate of NO₂ photoadsorption can be calculated. The temperature dependence of specific rate of NO₂ photoadsorption from an oxygen-rich atmosphere on the ZnO surface, calculated for three temperature points (31, 50, and 100 °C), lies near a straight line on the Arrhenius plot (Figure 14), which may indicate the activation nature of the process. The evaluated activation energies of photoactivated NO₂ binding on the ZnO are close values: 17 ± 2 meV (1.62 ± 0.2 kJ/mol) for ZnO-300 and 16 ± 2 meV (1.55 ± 0.2 kJ/mol) for ZnO-V_O.

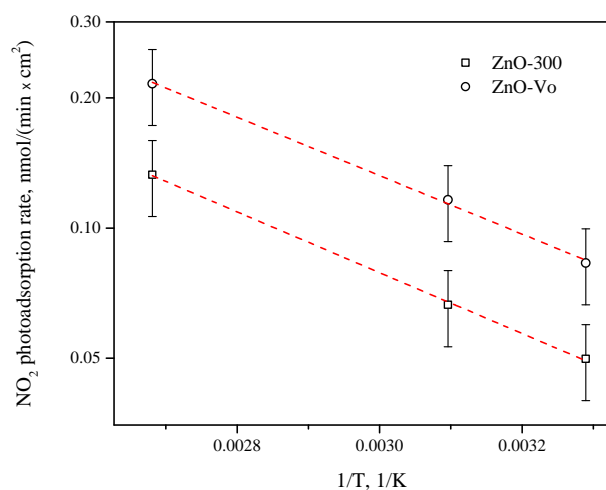
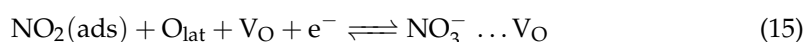
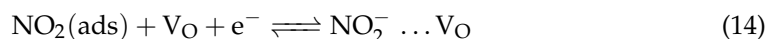


Figure 14. Temperature dependence of the rate of NO₂ photoadsorption under UV irradiation (370 nm) from an oxygen-rich atmosphere (He + 20% O₂ + 100 ppm NO₂) on the ZnO surface on the Arrhenius plot.

4.3. Insights to Mechanisms of Gas Sensitivity of ZnO to NO₂ under UV Activation

Since the NO₂ molecule is a strong electron acceptor, its adsorption is accompanied by the capture of electrons from the conduction band. The typical sites of adsorption of a NO₂ molecule on the ZnO surface are oxygen vacancies, on which, according to XPS and IR studies, near RT, a NO₂ molecule can orient itself in different ways, with the formation of NO₂⁻ and NO₃⁻ ions [29,56–61]. Thus, the sensor response to NO₂ requires both unoccupied adsorption sites and free electrons, which can be expressed by the following equations:



In dark at a constant temperature, equilibrium is established between the gaseous and adsorbed forms of NO₂ according to Equations (14) and (15). The maximum achievable value of the sensor signal to NO₂ in this case is controlled by the concentration of free electrons to the grains, which is not very high for nanocrystalline ZnO. As can be seen from Figure 11, the ZnO-300 and ZnO-V_O samples show a sensor response to NO₂ under dark conditions in the range of temperature of 30–100 °C, but the very high resistance ($R > 10^{10} \Omega$) of the sensor layers, bordering on dielectric properties, makes it difficult to measure. With increasing temperature, the resistance of the sensors slightly decreases due to an increase in the concentration of charge carriers by the mechanism of thermal activation; however, the surface concentration of NO₂ molecules decreases due to the predominant process of their thermal desorption. Thus, increasing the temperature does not appear to be a successful strategy for NO₂ sensor measurements in the dark.

When ZnO absorbs UV light, photoexcited charge carriers are generated, which leads to an activated surface state due to a sharp increase in the concentration of free electrons, which leads to a decrease in the base resistance to the order of $10^5 \Omega$. In this highly non-equilibrium state, the NO₂ adsorption rate increases dramatically, and NO₂ photoadsorption rate increases with increasing of temperature. Temperature change from 30 to 100 °C has little effect on the resistance of sensors under UV activation; however, it significantly enhances the NO₂ photoadsorption, which leads to its higher surface concentration on the sensor surface, and, as a result, a larger sensor signal can be achieved.

The abovementioned insights can be summarized by comparing the data of MS and sensor measurements of ZnO-300 and ZnO-V_O samples under UV photoactivation at in the temperature range of 30–100 °C (Figure 15). Two trends are obvious in these diagrams: (1) at the same temperature, the ZnO-V_O has a stronger photoadsorption and a higher sensor signal compared to ZnO-300 sample; (2) with increasing of temperature, rate of photoadsorption and the sensor signal increase for both ZnO-300 and ZnO-V_O samples.

The first trend is due to an increase in the reactivity of ZnO after post-annealing in an inert gas, which apparently causes an increase in the surface density of oxygen vacancies on the ZnO surface, which serve as adsorption sites for NO₂ molecules. The second trend is due to the activation nature of the interaction of NO₂ with the ZnO surface under UV irradiation. Thus, in both cases, there is a correlation between the ability of the ZnO sample to adsorb NO₂ and the sensor response to NO₂ under some conditions.

In other words, it follows from the obtained data that the sensor response of ZnO to NO₂ upon UV activation is proportional to the surface concentration of chemisorbed NO₂ molecules, which is reached upon detection. Thus, to design highly sensitive metal oxide sensors to NO₂, approaches can be used that include both modification of the sensing material to increase the density of adsorption sites (oxygen vacancies) on its surface, and variation of operation conditions, including the combination of light and moderate thermal activation.

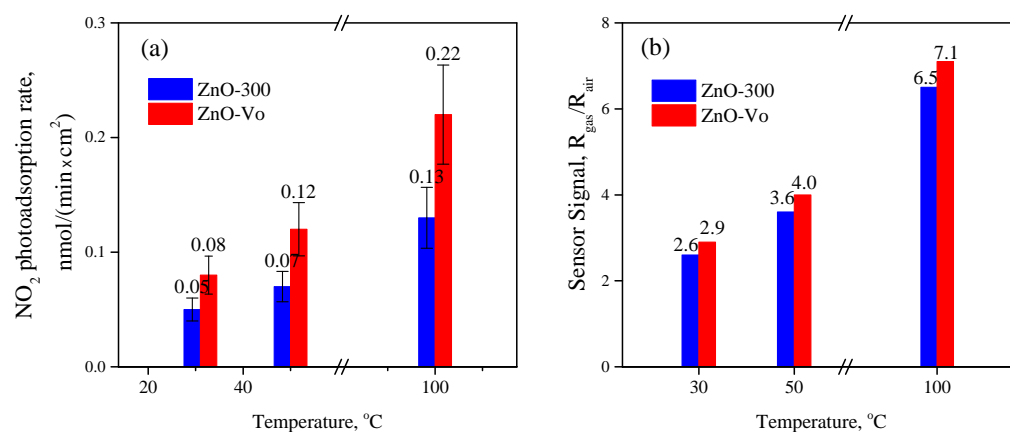


Figure 15. (a) Diagram shows the photoadsorption rate of NO₂ from an oxygen-rich atmosphere on ZnO-300 and ZnO-V_O samples at different temperatures (data extracted from graphs in Figure 9); (b) diagram shows sensor response of ZnO-300 and ZnO-V_O samples to 3.8 ppm NO₂ at different temperatures (data extracted from graphs in Figure 12).

5. Conclusions

In the present work, we studied photostimulated processes involving O₂ and NO₂ molecules on the ZnO surface by in situ MS in the temperature range of 31–100 °C under activation by UV radiation (370 nm). The synthesized nanocrystalline needle-shaped ZnO exhibits a sensor sensitivity to NO₂ when exposed to UV light, and, at the same time, it is characterized by photoadsorption of O₂ and NO₂. Upon post-annealing of the synthesized ZnO in an inert gas at 170 °C, a more active surface state is formed, which is most likely associated with an increase in the surface density of oxygen vacancies on the ZnO surface. This state is stable and provides high photoadsorption rates for O₂ and NO₂, as well as high sensor response values for NO₂ detection compared to as-prepared ZnO. It has been found that the process of NO₂ photoadsorption from an oxygen-rich atmosphere on the ZnO surface is an activation process in the temperature range of 31–100 °C, and activation energies have been determined for it. The obtained data show that for the studied ZnO-based sensor, there is a correlation between the ability to photoadsorb NO₂ and the sensor response to NO₂ under the same temperatures. Thus, in situ MS has great potential in the study of photostimulated chemical processes underlying the detection of various molecules by semiconductor gas sensors.

Supplementary Materials: The following are available online at <https://www.mdpi.com/article/10.3390/chemosensors10040147/s1>, Figure S1: Simulated test chamber airflow evolution during flow rate increase from 0 to 15 mL/min computed with OpenFOAM (boundary conditions: mass flow inlet, constant pressure outlet, no slip walls); Figure S2: Calibration curve showing the relationship between the concentration of NO₂ in the carrier gas and the ion current by $m/z = 30$; Figure S3: Thermal desorption of H₂O ($m/z = 18$ a.m.u.) and CO₂ ($m/z = 44$) from ZnO-300 sample in He flow at heating up to 150 °C.

Author Contributions: Conceptualization, A.C. and M.R.; methodology, A.C. and P.K.; software, P.K.; investigation, A.G., A.A., P.K. and A.C.; resources, M.R. and A.C.; writing—original draft preparation, A.C. and M.R.; writing—review and editing, A.C. and M.R.; project administration, A.C.; funding acquisition, A.C. All authors have read and agreed to the published version of the manuscript.

Funding: This research was funded by the Russian Science Foundation grant number 21-73-00157.

Institutional Review Board Statement: Not applicable.

Informed Consent Statement: Not applicable.

Data Availability Statement: The data presented in this study are available upon request from the corresponding author. The data are not publicly available due to privacy reasons.

Conflicts of Interest: The authors declare no conflicts of interest.

References

1. Moseley, P.T. Progress in the development of semiconducting metal oxide gas sensors: A review. *Meas. Sci. Technol.* **2017**, *28*, 082001. [[CrossRef](#)]
2. Korotcenkov, G.; Cho, B. Metal oxide composites in conductometric gas sensors: Achievements and challenges. *Sens. Actuators B* **2017**, *244*, 182–210. [[CrossRef](#)]
3. Barsan, N.; Koziej, D.; Weimar, U. Metal oxide-based gas sensor research: How to? *Sens. Actuators B* **2007**, *121*, 18–35. [[CrossRef](#)]
4. Rumyantseva, M.; Gas'kov, A. Chemical modification of nanocrystalline metal oxides: Effect of the real structure and surface chemistry on the sensor properties. *Russ. Chem. Bull.* **2008**, *57*, 1106–1125. [[CrossRef](#)]
5. Oprea, A.; Degler, D.; Barsan, N.; Hemeryck, A.; Rebholz, J. 3-Basics of semiconducting metal oxide-based gas sensors. In *Gas Sensors Based on Conducting Metal Oxides*; Metal Oxides; Barsan, N., Schierbaum, K., Eds.; Elsevier: Cambridge, MA, USA, 2019; pp. 61–165. [[CrossRef](#)]
6. Marikutsa, A.; Rumyantseva, M.; Konstantinova, E.A.; Gaskov, A. The Key Role of Active Sites in the Development of Selective Metal Oxide Sensor Materials. *Sensors* **2021**, *21*, 2554. [[CrossRef](#)]
7. Xue, S.; Cao, S.; Huang, Z.; Yang, D.; Zhang, G. Improving Gas-Sensing Performance Based on MOS Nanomaterials: A Review. *Materials* **2021**, *14*, 4263. [[CrossRef](#)]
8. Chizhov, A.; Rumyantseva, M.; Gaskov, A. Light Activation of Nanocrystalline Metal Oxides for Gas Sensing: Principles, Achievements, Challenges. *Nanomaterials* **2021**, *11*, 892. [[CrossRef](#)]
9. Wang, J.; Shen, H.; Xia, Y.; Komarneni, S. Light-activated room-temperature gas sensors based on metal oxide nanostructures: A review on recent advances. *Ceram. Int.* **2021**, *47*, 7353–7368. [[CrossRef](#)]
10. Xuan, J.; Zhao, G.; Sun, M.; Jia, F.; Wang, X.; Zhou, T.; Yin, G.; Liu, B. Low-temperature operating ZnO-based NO₂ sensors: A review. *RSC Adv.* **2020**, *10*, 39786–39807. [[CrossRef](#)]
11. Korotcenkov, G.; Cho, B.K. Engineering approaches for the improvement of conductometric gas sensor parameters: Part 1. Improvement of sensor sensitivity and selectivity (short survey). *Sens. Actuators B* **2013**, *188*, 709–728. [[CrossRef](#)]
12. Solomatin, M.A.; Glukhova, O.E.; Fedorov, F.S.; Sommer, M.; Shunaev, V.V.; Varezchnikov, A.S.; Nasibulin, A.G.; Ushakov, N.M.; Sysoev, V.V. The UV Effect on the Chemiresistive Response of ZnO Nanostructures to Isopropanol and Benzene at PPM Concentrations in Mixture with Dry and Wet Air. *Chemosensors* **2021**, *9*, 181. [[CrossRef](#)]
13. Kumar, R.; Liu, X.; Zhang, J.; Kumar, M. Room-Temperature Gas Sensors Under Photoactivation: From Metal Oxides to 2D Materials. *Nano-Micro Lett.* **2020**, *12*, 164. [[CrossRef](#)]
14. Xu, F.; Ho, H.P. Light-Activated Metal Oxide Gas Sensors: A Review. *Micromachines* **2017**, *8*, 333. [[CrossRef](#)]
15. Cheng, Y.; Ren, B.; Xu, K.; Jeerapan, I.; Chen, H.; Li, Z.; Ou, J.Z. Recent progress in intrinsic and stimulated room-temperature gas sensors enabled by low-dimensional materials. *J. Mater. Chem. C* **2021**, *9*, 3026–3051. [[CrossRef](#)]
16. Chizhov, A.; Rumyantseva, M.; Drozdov, K.; Krylov, I.; Batuk, M.; Hadermann, J.; Filatova, D.; Khmelevsky, N.; Kozlovsky, V.; Maltseva, L.; et al. Photoresistive gas sensor based on nanocrystalline ZnO sensitized with colloidal perovskite CsPbBr₃ nanocrystals. *Sens. Actuators B* **2021**, *329*, 129035. [[CrossRef](#)]
17. Baltrusaitis, J.; Jayaweera, P.M.; Grassian, V.H. XPS study of nitrogen dioxide adsorption on metal oxide particle surfaces under different environmental conditions. *Phys. Chem. Chem. Phys.* **2009**, *11*, 8295–8305. [[CrossRef](#)]

18. Karagoz, B.; Tsyshevsky, R.; Trotochaud, L.; Yu, Y.; Karshoğlu, O.; Blum, M.; Eichhorn, B.; Bluhm, H.; Kuklja, M.M.; Head, A.R. NO₂ Interactions with MoO₃ and CuO at Atmospherically Relevant Pressures. *J. Phys. Chem. C* **2021**, *125*, 16489–16497. [[CrossRef](#)]
19. Drozdowska, K.; Welearegay, T.; Osterlund, L.; Smulko, J. Combined chemoresistive and in situ FTIR spectroscopy study of nanoporous NiO films for light-activated nitrogen dioxide and acetone gas sensing. *Sens. Actuators B* **2022**, *353*, 131125. [[CrossRef](#)]
20. Chen, M.; Wang, Z.; Han, D.; Gu, F.; Guo, G. High-sensitivity NO₂ gas sensors based on flower-like and tube-like ZnO nanomaterials. *Sens. Actuators B* **2011**, *157*, 565–574. [[CrossRef](#)]
21. Sergent, N.; Epifani, M.; Pagnier, T. In situ Raman spectroscopy study of NO₂ adsorption onto nanocrystalline tin(IV) oxide. *J. Raman Spectrosc.* **2006**, *37*, 1272–1277. [[CrossRef](#)]
22. Wang, J.; Hu, C.; Xia, Y.; Zhang, B. Mesoporous ZnO nanosheets with rich surface oxygen vacancies for UV-activated methane gas sensing at room temperature. *Sens. Actuators B* **2021**, *333*, 129547. [[CrossRef](#)]
23. Sharma, A.; Rout, C.S. Advances in understanding the gas sensing mechanisms by in situ and operando spectroscopy. *J. Mater. Chem. A* **2021**, *9*, 18175–18207. [[CrossRef](#)]
24. Cho, I.; Sim, Y.C.; Cho, M.; Cho, Y.H.; Park, I. Monolithic Micro Light-Emitting Diode/Metal Oxide Nanowire Gas Sensor with Microwatt-Level Power Consumption. *ACS Sens.* **2020**, *5*, 563–570. [[CrossRef](#)] [[PubMed](#)]
25. Wang, J.; Yang, Y.; Xia, Y. Mesoporous MXene/ZnO nanorod hybrids of high surface area for UV-activated NO₂ gas sensing in ppb-level. *Sens. Actuators B* **2022**, *353*, 131087. [[CrossRef](#)]
26. Li, G.; Sun, Z.; Zhang, D.; Xu, Q.; Meng, L.; Qin, Y. Mechanism of Sensitivity Enhancement of a ZnO Nanofilm Gas Sensor by UV Light Illumination. *ACS Sens.* **2019**, *4*, 1577–1585. [[CrossRef](#)]
27. Fan, S.W.; Srivastava, A.K.; Dravid, V.P. UV-activated room-temperature gas sensing mechanism of polycrystalline ZnO. *Appl. Phys. Lett* **2009**, *95*, 142106. [[CrossRef](#)]
28. Ding, W.; Liu, D.; Liu, J.; Zhang, J. Oxygen Defects in Nanostructured Metal-Oxide Gas Sensors: Recent Advances and Challenges. *Chin. J. Chem.* **2020**, *38*, 1832–1846. [[CrossRef](#)]
29. Wang, J.; Shen, Y.; Li, X.; Xia, Y.; Yang, C. Synergistic effects of UV activation and surface oxygen vacancies on the room-temperature NO₂ gas sensing performance of ZnO nanowires. *Sens. Actuators B* **2019**, *298*, 126858. [[CrossRef](#)]
30. Gurylev, V.; Perng, T.P. Defect engineering of ZnO: Review on oxygen and zinc vacancies. *J. Eur. Ceram. Soc.* **2021**, *41*, 4977–4996. [[CrossRef](#)]
31. Kumar, R.R.; Murugesan, T.; Chang, T.W.; Lin, H.N. Defect controlled adsorption/desorption kinetics of ZnO nanorods for UV-activated NO₂ gas sensing at room temperature. *Mater. Lett.* **2021**, *287*, 129257. [[CrossRef](#)]
32. Zhang, C.; Li, Y.; Liu, G.; Liu, K.; Wu, K. Room temperature NO₂ sensing properties of ZnO_{1-ff} coating prepared by hydrogen reduction method. *Ceram. Int.* **2021**, *47*, 29873–29880. [[CrossRef](#)]
33. Paolucci, V.; De Santis, J.; Lozzi, L.; Rigon, M.; Martucci, A.; Cantalini, C. ZnO thin films containing aliovalent ions for NO₂ gas sensor activated by visible light. *Ceram. Int.* **2021**, *47*, 25017–25028. [[CrossRef](#)]
34. Li, G.; Zhang, H.; Meng, L.; Sun, Z.; Chen, Z.; Huang, X.; Qin, Y. Adjustment of oxygen vacancy states in ZnO and its application in ppb-level NO₂ gas sensor. *Sci. Bull.* **2020**, *65*, 1650–1658. [[CrossRef](#)]
35. Liu, J.; Gao, F.; Wu, L.; Zhang, H.; Hong, W.; Jin, G.; Zhai, Z.; Fu, C. Size effect on oxygen vacancy formation and gaseous adsorption in ZnO nanocrystallites for gas sensors: A first principle calculation study. *Appl. Phys. A* **2020**, *126*, 454. [[CrossRef](#)]
36. Lu, W.; Olaitan, A.D.; Brantley, M.R.; Zekavat, B.; Erdogan, D.A.; Ozensoy, E.; Solouki, T. Photocatalytic Conversion of Nitric Oxide on Titanium Dioxide: Cryotrapping of Reaction Products for Online Monitoring by Mass Spectrometry. *J. Phys. Chem. C* **2016**, *120*, 8056–8067. [[CrossRef](#)]
37. Bedjanian, Y.; El Zein, A. Interaction of NO₂ with TiO₂ Surface Under UV Irradiation: Products Study. *J. Phys. Chem. A* **2012**, *116*, 1758–1764. [[CrossRef](#)]
38. Sanchez-Martín, S.; Olaizola, S.; Castaño, E.; Mandayo, G.; Ayerdi, I. Low temperature NO₂ gas sensing with ZnO nanostructured by laser interference lithography. *RSC Adv.* **2021**, *11*, 34144–34151. [[CrossRef](#)]
39. Bobkov, A.; Varezchnikov, A.; Plugin, I.; Fedorov, F.S.; Trouillet, V.; Geckle, U.; Sommer, M.; Goffman, V.; Moshnikov, V.; Sysoev, V. The Multisensor Array Based on Grown-On-Chip Zinc Oxide Nanorod Network for Selective Discrimination of Alcohol Vapors at Sub-ppm Range. *Sensors* **2019**, *19*, 4265. [[CrossRef](#)]
40. Benamara, M.; Massoudi, J.; Dahman, H.; Ly, A.; Dhahri, E.; Debliquy, M.; El Mir, L.; Lahem, D. Study of room temperature NO₂ sensing performances of ZnO_{1-x} (x = 0, 0.05, 0.10). *Appl. Phys. A* **2022**, *128*, 31. [[CrossRef](#)]
41. Liu, K.; Sakurai, M.; Aono, M. ZnO-Based Ultraviolet Photodetectors. *Sensors* **2010**, *10*, 8604–8634. [[CrossRef](#)]
42. Soci, C.; Zhang, A.; Xiang, B.; Dayeh, S.A.; Aplin, D.P.R.; Park, J.; Bao, X.Y.; Lo, Y.H.; Wang, D. ZnO Nanowire UV Photodetectors with High Internal Gain. *Nano Lett.* **2007**, *7*, 1003–1009. [[CrossRef](#)]
43. Djurišić, A.; Leung, Y.H. Optical Properties of ZnO Nanostructures. *Small* **2006**, *2*, 944–961. [[CrossRef](#)]
44. Galdámez-Martínez, A.; Santana, G.; Güell, F.; Martínez-Alanis, P.R.; Dutt, A. Photoluminescence of ZnO Nanowires: A Review. *Nanomaterials* **2020**, *10*, 857. [[CrossRef](#)]
45. Janotti, A.; Van de Walle, C.G. Native point defects in ZnO. *Phys. Rev. B* **2007**, *76*, 165202. [[CrossRef](#)]
46. Chandrinou, C.; Boukos, N.; Stogios, C.; Travlos, A. PL study of oxygen defect formation in ZnO nanorods. *Microelectron. J.* **2009**, *40*, 296–298. [[CrossRef](#)]

47. Verma, S.; Jain, S.L. Nanosized zinc peroxide (ZnO₂): A novel inorganic oxidant for the oxidation of aromatic alcohols to carbonyl compounds. *Inorg. Chem. Front.* **2014**, *1*, 534–539. [[CrossRef](#)]
48. Janotti, A.; Van de Walle, C.G. Oxygen vacancies in ZnO. *Appl. Phys. Lett.* **2005**, *87*, 122102. [[CrossRef](#)]
49. Melnick, D.A. Zinc Oxide Photoconduction, an Oxygen Adsorption Process. *J. Chem. Phys.* **1957**, *26*, 1136–1146. [[CrossRef](#)]
50. Barry, T.I.; Stone, F.S. The Reactions of Oxygen at Dark and Irradiated Zinc Oxide Surface. *Proc. R. Soc. Lond. A Math. Phys. Sci.* **1960**, *255*, 124–144.
51. Yan, Y.; Al-Jassim, M.M.; Wei, S.H. Oxygen-vacancy mediated adsorption and reactions of molecular oxygen on the ZnO(10 $\bar{1}$ 0) surface. *Phys. Rev. B* **2005**, *72*, 161307. [[CrossRef](#)]
52. Klimovskii, A.; Lisachenko, A. Determination of the kinetic-parameters for the photoadsorption and photodesorption of oxygen on zinc-oxide. *Kinet. Catal.* **1991**, *32*, 373–377.
53. Titov, V.V.; Lisachenko, A.A.; Labzovskaya, M.E.; Akopyan, I.K.; Novikov, B.V. Exciton Channel of Photoactivation for Redox Reactions on the Surface of 2D ZnO Nanostructures. *J. Phys. Chem. C* **2019**, *123*, 27399–27405. [[CrossRef](#)]
54. Gurlo, A. Interplay between O₂ and SnO₂: Oxygen Ionosorption and Spectroscopic Evidence for Adsorbed Oxygen. *ChemPhysChem* **2006**, *7*, 2041–2052. [[CrossRef](#)] [[PubMed](#)]
55. Zhou, Y.; Wang, Y.; Wang, Y.; Li, X.; Guo, Y. The impact of carrier gas on room-temperature trace nitrogen dioxide sensing of ZnO nanowire-integrated film under UV illumination. *Ceram. Int.* **2020**, *46*, 16056–16061. [[CrossRef](#)]
56. Watanabe, K.; Matsumoto, K.; Ohgaki, T.; Sakaguchi, I.; Ohashi, N.; Hishita, S.; Haneda, H. Development of ZnO-based surface plasmon resonance gas sensor and analysis of UV irradiation effect on NO₂ desorption from ZnO thin films. *J. Ceram. Soc. Jpn.* **2010**, *118*, 193–196. [[CrossRef](#)]
57. Spencer, M.J.S.; Yarovsky, I. ZnO Nanostructures for Gas Sensing: Interaction of NO₂, NO, O, and N with the ZnO(1010) Surface. *J. Phys. Chem. C* **2010**, *114*, 10881–10893. [[CrossRef](#)]
58. Breedon, M.; Spencer, M.J.S.; Yarovsky, I. Adsorption of NO₂ on Oxygen Deficient ZnO(2 $\bar{1}$ $\bar{1}$ 0) for Gas Sensing Applications: A DFT Study. *J. Phys. Chem. C* **2010**, *114*, 16603–16610. [[CrossRef](#)]
59. Kaur, M.; Shaheera, M.; Pathak, A.; Gadkari, S.C.; Debnath, A.K. Highly sensitive NO₂ sensor based on ZnO nanostructured thin film prepared by SILAR technique. *Sens. Actuators B* **2021**, *335*, 129678. [[CrossRef](#)]
60. Chen, H.; Qu, Y.; Ding, J.; Fu, H. Adsorption behavior of graphene-like ZnO monolayer with oxygen vacancy defects for NO₂: A DFT study. *Superlattices Microstruct.* **2019**, *134*, 106223. [[CrossRef](#)]
61. Rodriguez, J.A.; Jirsak, T.; Dvorak, J.; Sambasivan, S.; Fischer, D. Reaction of NO₂ with Zn and ZnO: Photoemission, XANES, and Density Functional Studies on the Formation of NO₃. *J. Phys. Chem. C* **2000**, *104*, 319–328. [[CrossRef](#)]